Inorganic Chemistry

Article

pubs.acs.org/IC

Charge-Order Melting in Charge-Disproportionated Perovskite $CeCu_3Fe_4O_{12}$

Ikuya Yamada,*[,†,‡,§] Hidenobu Etani,[‡] Makoto Murakami,[∥] Naoaki Hayashi,[⊥] Takateru Kawakami,[#] Masaichiro Mizumaki,[∇,○] Shigenori Ueda,[◆] Hideki Abe,[§,¶] Klaus-Dieter Liss,[■] Andrew J. Studer,[■] Tomoatsu Ozaki,[∥,∞] Shigeo Mori,[∥] Ryoji Takahashi,[‡] and Tetsuo Irifune[▲]

[†]Nanoscience and Nanotechnology Research Center, Osaka Prefecture University, 1-2 Gakuen-cho, Naka-ku, Sakai, Osaka 599-8570, Japan

[‡]Department of Chemistry, Graduate School of Science and Engineering, Ehime University, 2-5 Bunkyo-cho, Matsuyama, Ehime 790-8577, Japan

[§]Precursory Research for Embryonic Science and Technology (PRESTO), Japan Science and Technology Agency (JST), 7 Goban-cho, Chiyoda-ku, Tokyo 102-0075, Japan

[∥]Department of Materials Science, Graduate School of Engineering, Osaka Prefecture University, 1-1 Gakuen-cho, Naka-ku, Sakai, Osaka 599-8531, Japan

[⊥]Institute for Integrated Cell-Material Sciences (iCeMS), Kyoto University, Yoshidaushinomiya-cho, Sakyo-ku, Kyoto 606-8501, Japan

[#]Department of Physics, College of Humanities and Sciences, Nihon University, 3-25-40 Sakurajosui, Setagaya-ku, Tokyo 156-8550, Japan

[∇]Japan Synchrotron Radiation Research Institute (JASRI), 1-1-1 Kouto, Sayo-cho, Sayo-gun, Hyogo 679-5198, Japan

[○]Core Research for Evolutional Science and Technology (CREST), JST, 7 Goban-cho, Chiyoda-ku, Tokyo 102-0075, Japan

[◆]Synchrotron X-ray Station at SPring-8, National Institute for Materials Science (NIMS), 1-1-1 Kouto, Sayo-cho, Sayo-gun, Hyogo 679-5148, Japan

[¶]Environmental Remediation Materials Unit, NIMS, 1-1 Namiki, Tsukuba 305-0044, Japan

[■]Bragg Institute, Australian Nuclear Science and Technology Organisation (ANSTO), Locked Bag 2001, Kirrawee DC, New South Wales 2232, Australia

[▲]Geodynamics Research Center (GRC), Ehime University, 2-5 Bunkyo-cho, Matsuyama, Ehime 790-8577, Japan

Supporting Information

ABSTRACT: A novel quadruple perovskite oxide $CeCu_3Fe_4O_{12}$ has been synthesized under high-pressure and high-temperature conditions of 15 GPa and 1473 K. ^{57}Fe Mössbauer spectroscopy displays a charge disproportionation transition of $4Fe^{3.5+} \rightarrow 3Fe^{3+} + Fe^{5+}$ below ~270 K, whereas hard X-ray photoemission and soft X-ray absorption spectroscopy measurements confirm that the Ce and Cu valences are retained at approximately +4 and +2, respectively, over the entire temperature range measured. Electron and X-ray diffraction studies reveal that the body-centered cubic symmetry (space group $Im\bar{3}$, No. 204) is retained at temperatures as low as 100 K, indicating the absence of any types of charge-ordering in the charge-disproportionated $CeCu_3Fe_4O_{12}$ phase. The magnetic susceptibility and neutron powder diffraction data illustrate that the antiferromagnetic ordering of Fe ions is predominant in the charge-disproportionated $CeCu_3Fe_4O_{12}$ phase. These findings suggest that $CeCu_3Fe_4O_{12}$ undergoes a new type of electronic phase in the $ACu_3Fe_4O_{12}$ series and that the melting of the charge-ordering in $CeCu_3Fe_4O_{12}$ is caused by the substantial decrease in the Fe valence and the resulting large deviation from the ideal abundance ratio of Fe^{3+}:Fe^{5+} = 1:1 for rock-salt-type charge-ordering.

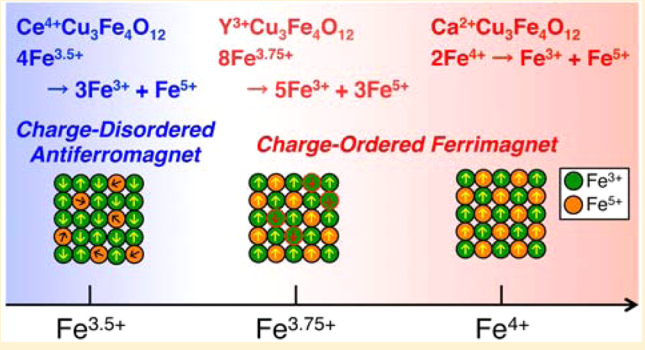

1. INTRODUCTION

The electronic properties of transition metal oxides have been widely investigated in the past decades, leading to the discovery

Received: September 2, 2014
Published: October 21, 2014

   dx.doi.org/10.1021/ic502138v | Inorg. Chem. 2014, 53, 11794−11801

of fascinating electronic properties, such as ferroelectricity, colossal magnetoresistance, and high-temperature superconductivity.[1] Perovskite-type transition metal oxides, ABO_3, are of particular interest owing to the high adjustability of their chemical compositions and crystal structures, which affect the electronic properties. Charge-ordering in mixed-valence transition metal ions play crucial roles in the aforementioned electronic properties: the ferroelectricity of ferrites,[2] colossal magnetoresistance of manganites,[3,4] and high-temperature superconductivity of cuprates;[5] thus, the order/disorder of charges by structural and electronic modifications is a topic of interest in solid state sciences.[6]

The quadruple perovskite oxide system $AA'_3B_4O_{12}$ attracts considerable attention because of its great diversity of structural and electronic properties, such as magnetoresistance, large dielectric constants, and heavy-Fermion-like behavior.[7−10] The manganites AMn_7O_{12} (A = Na^+, Ca^{2+}, La^{3+}), in which both the A′- and B-sites are occupied by Mn ions, illustrate the various structural and electronic phases associated with the charge/orbital orderings: monoclinic $Na^+(Mn^{3+}_3)(Mn^{3+}_2Mn^{4+}_2)O_{12}$ for $Mn^{3.5+}$ ions,[11] trigonal $Ca^{2+}(Mn^{3+}_3)(Mn^{3+}_3Mn^{4+}_1)O_{12}$ for $Mn^{3.25+}$ ions,[12] and monoclinic $La^{3+}(Mn^{3+}_3)(Mn^{3+}_4)O_{12}$ for single-valence Mn^{3+} ions.[13] For the former two of these, the 1:1- (rock-salt-type) and 3:1-type arrangements of Mn^{3+} and Mn^{4+} ions are dominated by the Jahn−Teller distortions of the Mn^{3+} ions.

Fascinating features involving charge-orderings are observed also in charge-disproportionated $ACu_3Fe_4O_{12}$ (ACFO, A = Ca^{2+}, Sr^{2+}, and trivalent rare-earth R^{3+}; see the crystal structure in Figure 1). The ACFO compounds contain unusual high-valence Fe^{4+} or $Fe^{3.75+}$ ions. The electronic states of the Fe^{4+} ions are dominated by ligand holes.[14] The Fe^{4+} ions have $d^5\underline{L}^1$ ($\underline{L}$: ligand hole) electron configurations rather than d^4, causing significant differences from isoelectronic Mn^{3+} (d^4) ions with Jahn−Teller activity. In the ACFO series, the electronic interactions between the B-site Fe^{4+} ($Fe^{3.75+}$) and A′-site Cu^{2+} ions induce interesting phenomena. $CaCu_3Fe_4O_{12}$ (CaCFO) undergoes a charge disproportionation ($2Fe^{4+} \rightarrow Fe^{3+} + Fe^{5+}$) transition with a rock-salt-type charge-ordering simultaneously with ferrimagnetic and metal−semiconductor transitions below 210 K.[15] A formally isoelectronic compound $SrCu_3Fe_4O_{12}$ displays a negative thermal expansion, which is induced by a continuous intersite charge transfer between the Cu and Fe ions ($3Cu^{2.4+} + 4Fe^{3.7+} \rightarrow 3Cu^{2.8+} + 4Fe^{3.4+}$) in a temperature range 170−270 K.[16,17] Recently, a systematic study on the $R^{3+}Cu^{2+}_3Fe^{3.75+}_4O_{12}$ (RCFO; R = Y, La, Pr, Nd, Sm, Eu, Gd, Tb, Dy, Ho, Er, Tm, Yb, Lu) revealed that the metal−oxygen bond strains dominate the types of electronic phase transitions; a couple of bond strains of overbonded R−O and underbonded Fe−O bonds induce intersite charge transfer transitions of $3Cu^{2+} + 4Fe^{3.75+} \rightarrow 3Cu^{3+} + 4Fe^{3+}$ for $R^{3+}Cu_3Fe_4O_{12}$ with larger R ions (R = La, Pr, Nd, Sm, Eu, Gd, Tb), whereas the opposite type of bond strains of underbonded R−O and overbonded Fe−O bonds result in charge disproportionation transitions of $8Fe^{3.75+} \rightarrow 5Fe^{3+} + 3Fe^{5+}$ for $R^{3+}Cu_3Fe_4O_{12}$ with smaller R ions (R = Y, Dy, Ho, Er, Tm, Yb, Lu).[18−20] A substantial difference between the charge-disproportionated phases of CaCFO and RCFO is the abundance ratios of Fe^{3+} and Fe^{5+} ions. Although the deviation from the ideal ratio for the rock-salt-type ordering (1:1) was considered as an essential factor destabilizing charge-ordered states at the early stage,[21,22] subsequent studies revealed that the charge-ordering is maintained in RCFO by substituting the excess Fe^{3+} ions for the Fe^{5+} ions.[19,20] A renewed area of interest in the charge-disproportionated ACFO system is what happens with further deviation from the ideal ratio of 1:1. Substitution of tetravalent ions such as Ce^{4+}, Te^{4+}, and Se^{4+} for A-site ions leading to the desired $A^{4+}Cu^{2+}_3Fe^{3.5+}_4O_{12}$ phase is necessary to answer the question. Until now, $CeCu_3Fe_4O_{12}$ (CeCFO) has been an unexplored compound although an experimental study on $CeCu_3Mn_4O_{12}$ was reported.[23]

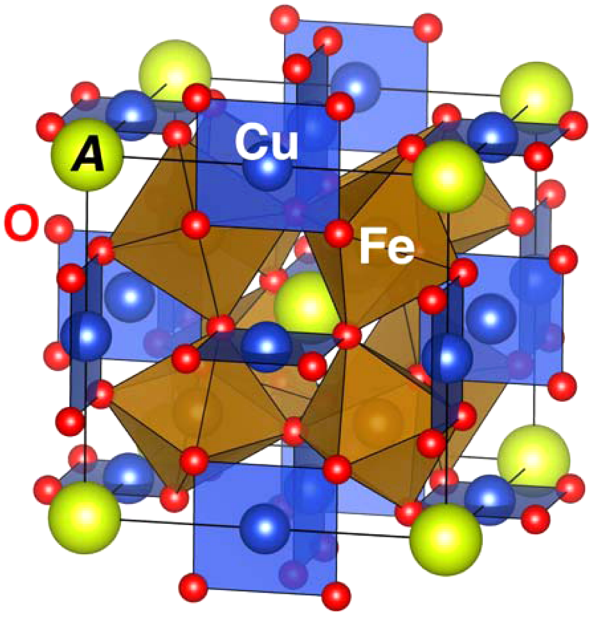

Figure 1. Crystal structure of $ACu_3Fe_4O_{12}$ (A = Ca, Sr, Y, lanthanides). Large yellow spheres, blue pseudosquare planes, and brown octahedra represent A ions, CuO_4 planar units, and FeO_6 octahedral units, respectively.

In this study, we examine the structural and electronic properties of a novel iron perovskite oxide CeCFO obtained using the high-pressure synthesis method. The room-temperature $Ce^{4+}Cu^{2+}_3Fe^{3.5+}_4O_{12}$ phase undergoes a charge disproportionation transition of $4Fe^{3.5+} \rightarrow 3Fe^{3+} + Fe^{5+}$ below ∼270 K. The crystal structure analyses on electron and X-ray diffraction data demonstrate that charge-ordering is melted in the charge-disproportionated phase of CeCFO. A G-type antiferromagnetic ordering of Fe^{3+} spins is predominant in the charge-disproportionated CeCFO phase rather than the ferrimagnetic ordering of Cu^{2+} and $Fe^{3+/5+}$ spins observed in the charge-ordered ACFO phase. These results indicate an intriguing structure−property relationship in the charge-disproportionated states.

2. EXPERIMENTAL SECTION

A precursor was prepared using the polymerized complex method.[24] Stoichiometric amounts of CeO_2 (99.9%), $Cu(NO_3)_2{\cdot}3H_2O$ (99.9%), and $Fe(NO_3)_3{\cdot}9H_2O$ (99.9%) were dissolved in nitric acid, to which a 5-fold excess of citric acid and a one-fold excess of 1,2-ethanediol were added while stirring. The resulting solution was heated to 573 K, while being stirred, and maintained at this temperature for 1 h to dry. Subsequently, the dried powder was fired using a furnace at 673 K for 1 h and 948 K for 12 h in air with occasional grindings. The obtained precursor with a nominal chemical composition of $CeCu_3Fe_4O_{11}$ was mixed with an oxidizing agent $KClO_4$ (99.9%) in a molar ratio of 2:1. The sample mixture was sealed off during the treatment in a platinum capsule with an inner diameter of 2.3 mm and a height of 4.0 mm. The capsule was placed into a (Mg,Co)O pressure medium and

dx.doi.org/10.1021/ic502138v | Inorg. Chem. 2014, 53, 11794−11801

compressed to 15 GPa using a high-pressure apparatus. The sample was subsequently heated to 1473 K in 20 min, maintained at this temperature for 30 min, and quenched to room temperature. During the heat treatment, the pressure was maintained at 15 GPa. The pressure was slowly released after the heat treatment. The obtained polycrystalline sample was washed several times with water, ethanol, and acetone.

Synchrotron X-ray powder diffraction (SXRD) experiments were performed at the beamline BL02B2 of SPring-8, Japan, using samples contained in Lindemann glass capillary tubes with an inner diameter of 0.2 mm. The wavelength used was determined to be 0.420 19 Å using a CeO_2 standard. Structure parameters were refined by Rietveld analysis using the program RIETAN-FP.[25] The crystal structures were drawn using the VESTA software.[26] No absorption correction was considered in the refinement, because the absorption effect was expected to be negligible. Electron diffraction (ED) patterns were collected at 300 and 100 K using a transmission electron microscope (JEM-2010). NPD data were collected between 6 and 300 K using the WOMBAT diffractometer at ANSTO.[27] The wavelength was 1.545 Å. The powder sample, having a mass of approximately 200 mg, was charged inside a vanadium can. The temperature was controlled using a cryorefrigerator from AS Scientific Products. The magnetic structure refinement was conducted using RIETAN-FP.[25]

^{57}Fe Mössbauer spectroscopy measurements were performed in transmission geometry using ^{57}Co/Rh as a radiation source and α-Fe as a control for the velocity calibration and isomer shift. The collected Mössbauer spectra were fitted computationally using the Lorentzian function. Hard X-ray photoemission spectroscopy (HAXPES) measurements were performed using a high-resolution hemispherical electron analyzer (VG SCIENTA R4000) installed at the undulator beamline BL15XU of SPring-8.[28,29] The incident photon energy was set to 5.95 keV. The total energy resolution was 235 meV, which was confirmed by the Fermi cutoff of an evaporated Au film. The binding energy was referred to the Fermi level of the Au film. The HAXPES spectra for the Ce 3d and Cu 2p core levels and the valence-band were collected at 20, 200, and 300 K. Soft X-ray absorption spectroscopy (XAS) for the Cu $L_{2,3}$ edge was measured at 15 and 300 K using a total electron yield method at the beamlines BL25SU[30] and BL27SU of SPring-8. Magnetization measurements were conducted using a superconducting quantum interference device (SQUID, Quantum Design MPMS-XL) between 5 and 300 K under external magnetic fields between 0.1 and 50 kOe. The electrical resistivity was measured by the standard four-probe method using a Quantum Design Physical Properties Measurement System (Quantum Design PPMS).

3. RESULTS AND DISCUSSION

Crystal Structures. A polycrystalline sample of CeCFO was successfully obtained in almost a single phase. Figure 2a shows the SXRD pattern at 300 K and the Rietveld refinement result. The Bragg reflection peaks from the primary phase could be indexed in the cubic $AA'_3B_4O_{12}$-type perovskite structure with a lattice constant of a = 7.352 57(8) Å, and the small peaks were attributed to α-Fe_2O_3 (ca. 4 wt %), CeO_2 (ca. 2 wt %), and unknown impurity phase(s) (presumably a few % at most). The ED patterns at 300 K were indexed with the space group $Im\bar{3}$ (No. 204), as shown in Figure 3. Therefore, the Rietveld refinement of the SXRD data was conducted in the $Im\bar{3}$ space group. The structure parameters obtained from the refinement are listed in Table 1. The reliability factors and goodness-of-fit (GOF) of R_{wp} = 4.495%, R_B = 1.667%, and GOF = 1.0240 suggest that the refinement results are satisfactory. The bond lengths and bond angle calculated from the refined structure parameters are listed in Table 2. The bond valence sum (BVS)[31] values of Cu and Fe were calculated using the formula BVS = $\sum_i^n \exp((r_0 - r_i)/B)$, where B is a constant (= 0.37), n is the number of bonds, r_0 is a parameter for the relevant bond, and r_i is the bond length. The BVS of Cu was calculated as

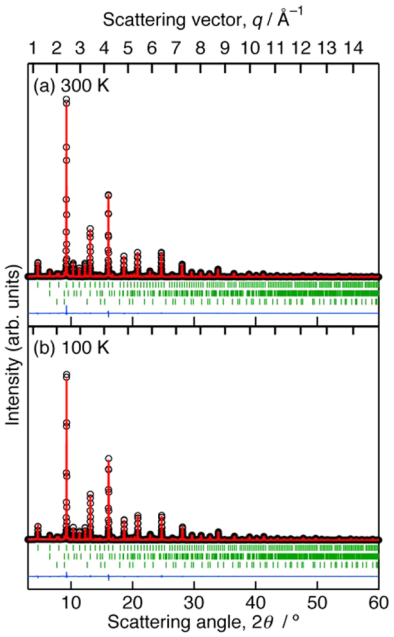

Figure 2. Observed and calculated SXRD profiles for $CeCu_3Fe_4O_{12}$ at (a) 300 K and (b) 100 K. The green vertical marks indicate the Bragg reflection positions of $CeCu_3Fe_4O_{12}$ (upper), α-Fe_2O_3 (middle), and CeO_2 (lower). Black markers and red lines indicate observed and calculated profiles, respectively. Blue bottom curve indicates the difference between observed and calculated profiles. The wavelength was 0.420 19 Å.

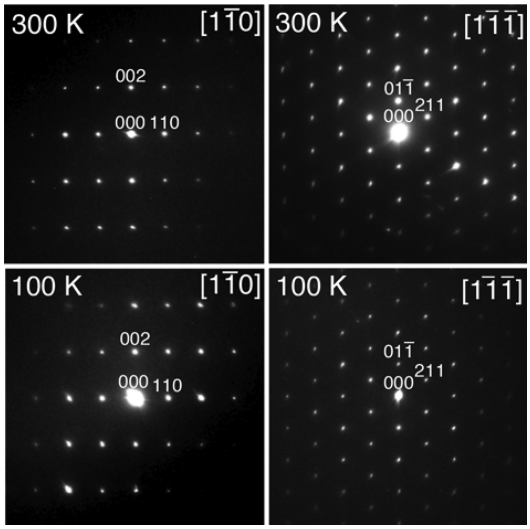

Figure 3. ED patterns along [1$\bar{1}$0] and [1$\bar{1}\bar{1}$] incidences at 100 and 300 K.

+1.98, suggesting a pure divalent state, whereas the BVS of Fe (+3.63) implies an intermediate valence state between +3 and +4, which is expected from the substitution of Ce^{4+} ions for R^{3+} ions. The BVS of Ce was tentatively calculated using the BVS parameters for the Ce^{3+}–O^{2-} (r_0 = 2.151 Å) and Ce^{4+}–O^{2-} (r_0 = 2.028 Å) bonds, resulting in BVS of +4.03 and +2.89, respectively. The corresponding bond discrepancies, $d_M = V_M$ − BVS(M), where V_M is the formal valence of the M ion, were calculated. The obtained values of $d_{Ce^{3+}}$ = +1.03 and $d_{Ce^{4+}}$ = −1.11 may represent excessive overbonding and underbonding, respectively, hampering the accurate estimation of the formal valence of the Ce ions. The Ce–O bond length (2.5551 Å) of

dx.doi.org/10.1021/ic502138v | Inorg. Chem. 2014, 53, 11794–11801

Table 1. Refined Structure Parameters for $CeCu_3Fe_4O_{12}$ at 100, 300, and 450 K Obtained from SXRD Data[a]

	100 K	300 K	450 K
a (Å)	7.339 08(8)	7.352 57(8)	7.366 36(9)
x (O)	0.3005(2)	0.3009(2)	0.3010(2)
y (O)	0.1741(2)	0.1739(2)	0.1743(2)
U_{iso}(Ce) (Å^2)	0.0168(11)	0.003 65(12)	0.005 69(14)
U_{iso}(Cu) (Å^2)	0.0224(10)	0.004 70(11)	0.007 15(13)
U_{iso}(Fe) (Å^2)	0.000 69(8)	0.002 00(9)	0.003 33(10)
U_{iso}(O) (Å^2)	0.0041(4)	0.0066(5)	0.0094(5)
R_{wp} (%)	4.825	4.495	4.450
R_B (%)	2.183	1.667	1.831
GOF	1.0682	1.0240	1.0488

[a]Space group: $Im\bar{3}$ (No. 204); atomic sites: Ce 2*a* (0, 0, 0), Cu 6*b* (0, $^1/_2$, $^1/_2$), Fe 8*c* ($^1/_4$, $^1/_4$, $^1/_4$), O 24*g* (*x*, *y*, 0). The occupancy factor *g* for all sites was fixed at unity.

Table 2. Selected Bond Lengths, Angles, and BVS Values for Metal Ions in $CeCu_3Fe_4O_{12}$ at 100, 300, and 450 K

	100 K	300 K	450 K
Ce−O (×12) (Å)	2.5487(16)	2.5551(15)	2.5617(15)
Cu−O (×4) (Å)	1.9433(16)	1.9438(15)	1.9488(15)
Cu−O (×4) (Å)	2.8045(17)	2.8094(16)	2.8120(16)
Fe−O (×6) (Å)	1.9530(6)	1.9575(5)	1.9605(5)
Fe−O−Fe (deg)	139.92(9)	139.78(9)	139.89(9)
BVS(Cu)	1.98	1.98	1.95
BVS(Fe)	3.68	3.63	3.60

[a]The BVS values were calculated using the following parameters: b_0 = 0.37 for all atoms, r_0 = 1.649 for Cu, and r_0 = 1.772 for Fe.

CeCFO is close to that of $CeCu_3Mn_4O_{12}$ (2.524 Å)[23] and almost identical with the sum of ionic radii[32] of Ce^{4+} (1.14 Å) and O^{2-} (1.40 Å) ions rather than that of Ce^{3+} (1.34 Å) and O^{2-} ions, implying that the Ce valence of CeCFO is tetravalent at room temperature.

The temperature dependence of the lattice constant *a* exhibits a monotonic thermal expansion, as shown in Figure 4a. No additional reflection spots were observed in the ED patterns upon cooling from 300 to 100 K; thus, the ED patterns of CeCFO at 100 K were indexed in the space group $Im\bar{3}$ (see Figure 3). This is in contrast with the symmetry lowering from $Im\bar{3}$ to $Pn\bar{3}$ (No. 201) in the previously reported charge disproportionation with rock-salt-type charge-ordering in ACFO (A = Ca^{2+}, R^{3+}).[15,19] The Rietveld refinement of the SXRD data was performed in the $Im\bar{3}$ space group at all measured temperatures. A reliable refinement result was indicated by the SXRD data at 100 K (Figure 2b). Figure 4b,c shows the temperature dependence of the metal−oxygen bond lengths calculated using the Rietveld refinement results. All of them indicate a monotonic increase with the temperature, and no anomalies were observed, implying the absence of intersite charge transfer between the constituent metal ions.

Valence States. The temperature evolution of the Fe valence was investigated by ^{57}Fe Mössbauer spectroscopy. Figure 5 shows Mössbauer spectra, and Table 3 lists the hyperfine parameters obtained from the fitting. The primary component with an isomer shift (IS) of 0.21 mm/s at 300 K is assigned to high-valence Fe ions at B-sites. This IS value is close to but slightly larger than those (0.16−0.18 mm/s) of the $R^{3+}Cu_3^{2+}Fe_4^{3.75+}O_{12}$ phases,[19,20] indicating that the Fe valence of CeCFO is smaller than +3.75. The second component (IS = 0.40 mm/s) has a large quadrupole splitting (ΔE_q) of 1.74 mm/s, attributed to the small amount of Fe^{3+} ions incorporated into the A′-sites, as in other types of ACFO.[15,16,19] Because the amount of Fe^{3+} ions at the A′-sites is negligible (1%), there are

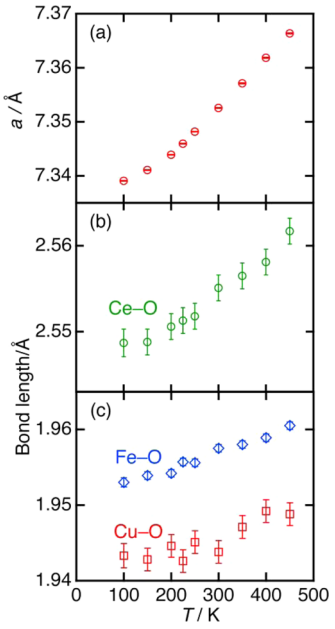

Figure 4. Temperature dependence of the (a) lattice constant *a*, (b) Ce−O, and (c) Cu−O, Fe−O bond lengths.

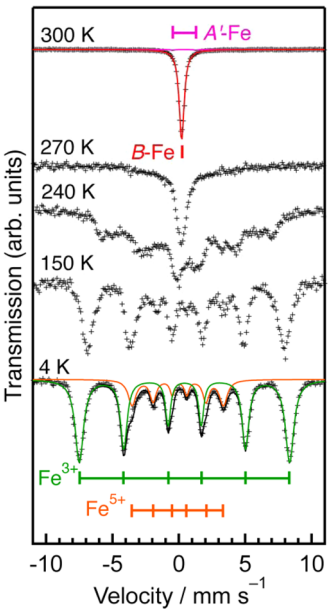

Figure 5. Mössbauer spectra at temperatures between 4 and 300 K for $CeCu_3Fe_4O_{12}$. Crosses and solid lines represent observed spectra and fittings, respectively.

Table 3. Hyperfine Parameters for $CeCu_3Fe_4O_{12}$ at 4 and 300 K Deduced from Mössbauer Spectra

	species	IS (mm/s)	HF (kOe)	ΔE_q (mm/s)	at. ratio (%)
300 K	B-Fe	0.21	0	0	99
	A′-Fe	0.40	0	1.74	1
4 K	Fe^{3+}	0.43	491	−0.01	77
	Fe^{5+}	−0.02	213	−0.13	23

dx.doi.org/10.1021/ic502138v | Inorg. Chem. 2014, 53, 11794−11801

insignificant effects on the essential electronic properties. The primary component is split into two sextet components upon cooling from 270 to 240 K. The IS values for these components at 4 K (0.43 and −0.02 mm/s) are, respectively, close to those of Fe^{3+} (ca. 0.40 mm/s) and Fe^{5+} (ca. 0.05 mm/s) ions,[15,16,19,20] indicating a charge disproportionation transition into Fe^{3+} and Fe^{5+} ions. The abundance ratio of Fe^{3+}:Fe^{5+} is 77:23 at this temperature. This value is significantly different from that of the charge-disproportionated RCFO (Fe^{3+}:Fe^{5+} = 62.5:37.5).[19,20] The average Fe valence of the charge-disproportionated CeCFO was calculated as approximately +3.5. Note that all other Fe^{3+} components were absent in the charge-disproportionated CeCFO, although two types of Fe^{3+} components were assigned to the Fe^{3+} ions occupying the original Fe^{3+} and Fe^{5+} sites, respectively, for RCFO.[19,20] This indicates that the Fe^{3+} and Fe^{5+} ions are randomly distributed in CeCFO, unlike the rock-salt-type charge-ordering for ACFO (A = Ca, Y, Dy−Lu).[15,19,20] This result is consistent with the crystal structure refinement results indicating the absence of the symmetry changes.

The valence states of the Ce and Cu ions in CeCFO were examined by HAXPES and XAS. Figure 6a shows the Ce 3d HAXPES spectra. The spectrum at 300 K exhibited a complicated spectral line shape and an intense peak at a binding energy of ∼916 eV, which is characteristic for the spectra of Ce^{4+}-oxides.[33] The entire spectral shape was retained at temperatures as low as 20 K, indicating that the Ce^{4+} valence is predominant between 20 and 300 K for CeCFO. The Ce^{4+} ions at the A-sites in the perovskite oxides are uncommon; thus, the carrier doping by the substitution of Ce^{4+} ions for R^{3+} ions may induce the essential change of electronic states in ACFO series. Figure 6b shows the HAXPES spectra of the Cu 2p core level. The spectral shape with a distinctive shakeup satellite at a binding energy of ∼935 eV is similar to those of typical Cu^{2+}-oxides.[34] The entire spectral shape remained unchanged upon cooling to 20 K. Figure 6d shows the Cu $L_{2,3}$-edge XAS spectra at 15 and 300 K. The sharp single peak at the L_3 edge is located at ∼931 eV at 15 and 300 K, confirming that the Cu valence is +2. On the basis of the HAXPES and XAS analyses, we conclude that the Cu^{2+} valence is retained for CeCFO over the entire temperature range measured, regardless of the charge disproportionation. Therefore, the charge disproportionation transition of CeCFO can be represented as $Ce^{4+}Cu^{2+}{}_3Fe^{3.5+}{}_4O_{12} \rightarrow Ce^{4+}Cu^{2+}{}_3(Fe^{3+}{}_3Fe^{5+}{}_1)O_{12}$. This is a new type of electronic transformation in the ACFO series.

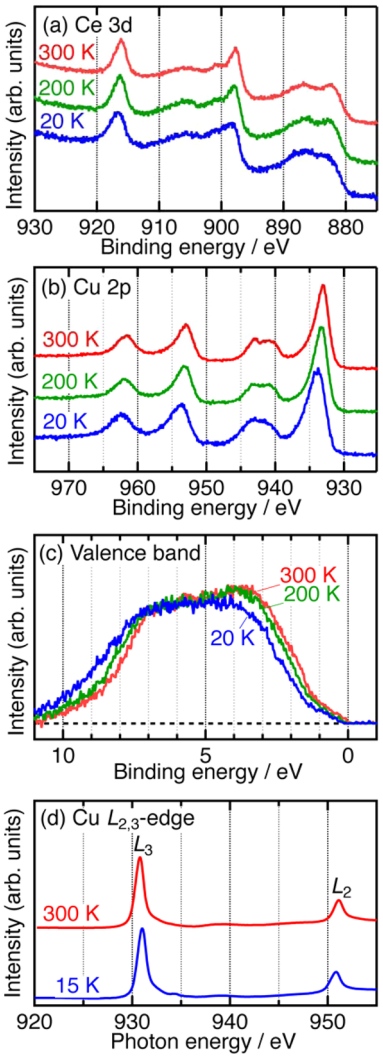

Figure 6. HAXPES spectra of (a) Ce 3d, (b) Cu 2p, and (c) valence band at 20, 200, and 300 K for $CeCu_3Fe_4O_{12}$. (d) XAS spectra of Cu $L_{2,3}$-edge at 15 and 300 K for $CeCu_3Fe_4O_{12}$.

Magnetic and Electrical Properties. Figure 7a shows the temperature dependence of the magnetic susceptibility of CeCFO in various external magnetic fields. Antiferromagnetic transitions with cusps were observed at 260−280 K, which slightly varied with the magnetic fields, followed by the deviations between the zero-field cooling (ZFC) and field cooling (FC) modes below the transition temperatures. The large upturns below ∼100 K under low magnetic fields are

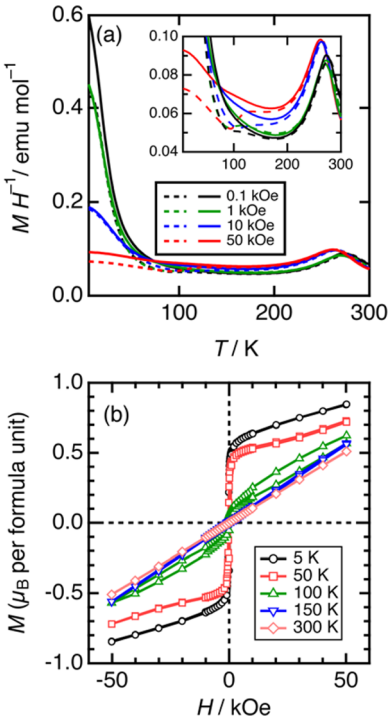

Figure 7. (a) Temperature dependence of the magnetic susceptibility of $CeCu_3Fe_4O_{12}$ measured in various external magnetic fields on ZFC (dashed lines) and FC (solid lines) between 5 and 300 K. The inset shows the enlarged data. (b) Isothermal magnetization curves measured at temperatures between 5 and 300 K after ZFC.

dx.doi.org/10.1021/ic502138v | Inorg. Chem. 2014, 53, 11794−11801

attributed to ferromagnetic-like domains, as discussed later. Figure 8a shows the NPD patterns of CeCFO in a selected 2θ (q) range at temperatures between 6 and 300 K. The magnetic 111 Bragg reflection appeared, and the intensity of the 113 reflection significantly increased below 280 K, suggesting that a long-range magnetic ordering is predominant in the charge-disproportionated CeCFO phase. The situation is similar to the antiferromagnetic $La^{3+}Cu^{3+}{}_3Fe^{3+}{}_4O_{12}$ phase, in which the Fe^{3+} ($S = {}^5/_2$) spins are ordered in a G-type antiferromagnet. Thus, we assume the G-type antiferromagnetism with the Fe spins aligned antiparallel along the c axis, with a propagation vector of $\mathbf{k} = 0$ in the magnetic structure refinement of CeCFO, yields reliable results (R_{wp} = 4.485%, R_{nuc} = 1.159%, R_{mag} = 1.181%, and GOF = 2.817 for 6 K) as shown in Figure 8b. Figure 8c shows the temperature dependence of the refined Fe magnetic moment for CeCFO. The Fe magnetic moment at 6 K was 2.27(4) μ_B, which is far smaller than the theoretical value for Fe^{3+} ions (5 μ_B, $S = {}^5/_2$). This is because the Fe^{5+} ions occupying one-quarter of the Fe sites probably do not contribute to the antiferromagnetic ordering. The randomly distributed Fe^{5+} ions are also expected to disturb the antiferromagnetic superexchange interactions in the Fe^{3+}−O−Fe^{3+} pathway,[35] leading to partially magnetic disordered states between neighboring Fe^{3+} and Fe^{5+} ions. This is supported by the large deviations between the ZFC and FC modes below ∼130 K in the magnetic susceptibility data, as previously mentioned (Figure 7a). The magnetic ordered states of the Cu^{2+} spins ($S = {}^1/_2$) are difficult to be precisely determined, using the present NPD data. We speculate that the Cu spins are in disordered states because the antiferromagnetic ordering of the B-site spins does not promote the ferromagnetic/antiferromagnetic alignment of A′-site spins.[11,36] Figure 7b indicates the isothermal magnetization (M−H) curves of CeCFO at temperatures between 5 and 300 K. Linear M−H curves were observed at 200 and 300 K. Below the large ZFC-FC deviation temperature (∼150 K), nonlinear M−H curves were observed. The M−H curve at 5 K exhibited an apparent spontaneous-magnetization-like behavior with a very small value (∼0.8 μ_B). This is attributed to the small amount of ferromagnetic-like domains with partial orderings of Fe^{3+} and Fe^{5+} ions in small scales, in which ferromagnetic superexchange interactions in the Fe^{3+}−O−Fe^{5+} bonds are expected.[35]

The electrical resistivity of CeCFO was semiconductor-like between 2 and 300 K (Figure 9), in contrast with the metal-to-nonmetal transitions associated with the charge disproportionation transitions for ACFO (A = Ca, R).[15,19,20] We speculate that the intrinsic character of CeCFO was obscured by extrinsic effects such as the grain boundary conduction. A high-quality single crystalline sample is needed to unveil the intrinsic electrical transport property of CeCFO. The valence-band HAXPES spectra (Figure 6c) exhibit an obvious gap-opening at the Fermi energy, with a rigid-band-like shifting by ∼1 eV from 300 to 20 K, revealing that the electronic structure in the vicinity of the Fermi energy changes from metallic to nonmetallic upon cooling.

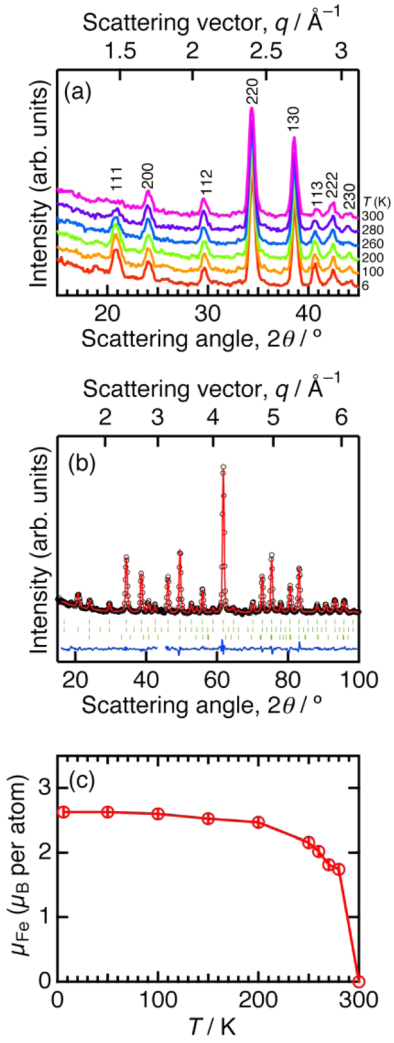

Figure 8. (a) Observed NPD patterns at temperatures between 6 and 300 K for $CeCu_3Fe_4O_{12}$. The wavelength was 1.545 Å. (b) Observed and calculated NPD profiles for $CeCu_3Fe_4O_{12}$ at 6 K. The green vertical marks indicate the Bragg reflection positions of the nuclear (upper) and magnetic (middle) diffractions of $CeCu_3Fe_4O_{12}$, and α-Fe_2O_3 (lower). Black markers and red lines indicate observed and calculated profiles, respectively. Blue bottom curve indicates the difference between observed and calculated profiles. The wavelength was 1.545 Å. (c) Temperature dependence of the refined magnetic moment of Fe ions (μ_{Fe}) for $CeCu_3Fe_4O_{12}$.

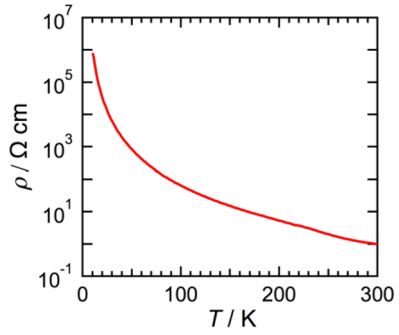

Figure 9. Temperature dependence of the electrical resistivity for $CeCu_3Fe_4O_{12}$.

Structure−Property Relationship. The crystal structures, valence states, and physical properties of the charge-disproportionated CeCFO are distinguished from those of previously reported charge-disproportionated ACFO compounds. Figure 10 presents a schematic of the charge-disproportionated phases of the ACFO series (A = Ca, Y, Ce). The Cu valences are always retained at approximately +2 in this series, whereas the Fe valences decrease from +4 (A =

dx.doi.org/10.1021/ic502138v | Inorg. Chem. 2014, 53, 11794−11801

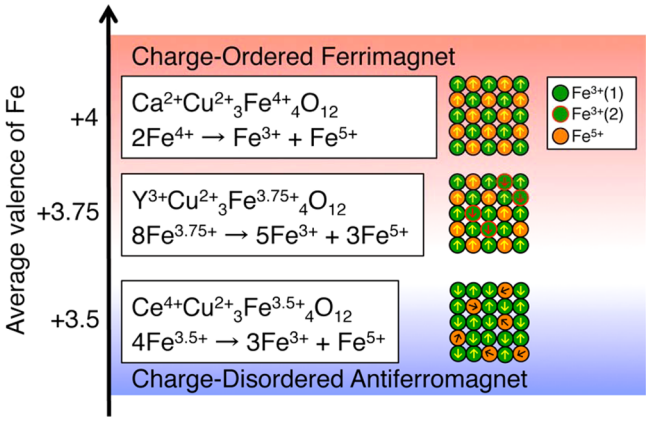

Figure 10. Schematic picture of the charge-disproportionated phases of $ACu_3Fe_4O_{12}$ (A = Ca, Y, Ce). The arrows represent the directions of Fe spins.

Ca) to +3.75 (A = Y) and then to +3.5 (A = Ce). The unusual high-valence Fe ions disproportionate into Fe^{3+} and Fe^{5+} ions at low temperatures. The abundance ratios of Fe^{3+}:Fe^{5+} systematically change with the formal Fe valence from ~50:50 (1:1) for A = Ca to ~62.5:37.5 (5:3) for A = Y and then to ~75:25 (3:1) for A = Ce. The ideal abundance ratio for the rock-salt-type charge-ordering is achieved in CaCFO. The same charge-ordering pattern is maintained for YCFO, in which the excess Fe^{3+} ions are incorporated into the Fe^{5+} sites. CeCFO exhibits a further deviation from 1:1; thus, rock-salt-type charge-ordering is not tolerated. Another type of charge-ordering, layered Fe^{3+}–Fe^{3+}–Fe^{5+}-type (2:1-type)[37] in $La_{0.7}Sr_{0.3}FeO_3$, seems not to be stabilized in the $AA'_3B_4O_{12}$-type structure, probably because of the instability of the symmetry lowering from $Im\bar{3}$. The 3:1-type charge-ordering, i.e., that of trigonal $CaMn_7O_{12}$, is not also applicable for CeCFO, because flexible octahedral distortions with Jahn–Teller activity are prohibited for non-Jahn–Teller Fe^{3+} and Fe^{5+} ions in almost regular FeO_6 octahedra. Therefore, the rock-salt-type charge-ordering is the only possible pattern in the cubic ACFO perovskites, and the large deviation from the 1:1 abundance ratio melts the ordering. Further investigations of solid solutions among CaCFO, YCFO, and CeCFO are in progress, wherein the formal Fe valence can be precisely controlled between +4 and +3.5.

4. SUMMARY

In summary, a novel $AA'_3B_4O_{12}$-type iron perovskite oxide $CeCu_3Fe_4O_{12}$ was synthesized in high-pressure and high-temperature conditions. Mössbauer, HAXPES, and XAS spectroscopic measurements revealed that this compound has a valence state of $Ce^{4+}Cu^{2+}{}_3Fe^{3.5+}{}_4O_{12}$ at room temperature and transforms into a charge-disproportionated and charge-disordered phase of $Ce^{4+}Cu^{2+}{}_3(Fe^{3+}{}_3Fe^{5+}{}_1)O_{12}$ below ~270 K. $CeCu_3Fe_4O_{12}$ shows an antiferromagnetic transition almost simultaneously with the charge disproportionation, in contrast with the ferromagnetic properties of charge-disproportionated and charge-ordered $ACu_3Fe_4O_{12}$ phases. This finding indicates that the melting of the charge-ordering in the $ACu_3Fe_4O_{12}$ system is driven by decrease in the Fe valence to ~3.5.

■ ASSOCIATED CONTENT

Ⓢ Supporting Information

Crystallographic data (CIF) for $CeCu_3Fe_4O_{12}$. This material is available free of charge via the Internet at http://pubs.acs.org.

■ AUTHOR INFORMATION

Corresponding Author

*E-mail: i-yamada@21c.osakafu-u.ac.jp.

Present Address

[∞]Technology Research Institute of Osaka Prefecture, Izumi, Japan.

Notes

The authors declare no competing financial interest.

■ ACKNOWLEDGMENTS

The synchrotron radiation experiments were performed at SPring-8 with the approval of JASRI (Proposal Nos. 2012A1002, 2012B1171, 2013B1063, 2014A1206, and 2014A1224) and NIMS Synchrotron X-ray Station (Proposal Nos. 2013A4600 and 2013B4905). The authors are grateful to HiSOR, Hiroshima University, and JAEA/SPring-8 for the development of HAXPES at BL15XU of SPring-8. The NPD experiment was conducted at ANSTO (Proposal No. P3468), which was transferred from HERMES with the approval of Institute for Solid State Physics, The University of Tokyo (Proposal No. NSL-00000195), JAEA, Tokai, Japan. This work was performed under the Visiting Researcher's Program of Geodynamics Research Center, Ehime University. This work was partially supported by the Murata Science Foundation and Nanotechnology Platform (Project No. 12024046) of the Ministry of Education, Culture, Sports, Science and Technology, Japan.

■ REFERENCES

(1) Imada, M.; Fujimori, A.; Tokura, Y. *Rev. Mod. Phys.* **1998**, *70*, 1039–1263.
(2) Ikeda, N.; Ohsumi, H.; Ohwada, K.; Ishii, K.; Inami, T.; Kakurai, K.; Murakami, Y.; Yoshii, K.; Mori, S.; Horibe, Y.; Kito, H. *Nature* **2005**, *436*, 1136–1138.
(3) Bao, W.; Axe, J. D.; Chen, C. H.; Cheong, S. W. *Phys. Rev. Lett.* **1997**, *78*, 543–546.
(4) Rao, C. N. R.; Cheetham, A. K. *Science* **1997**, *276*, 911–912.
(5) Kumar, N.; Rao, C. N. R. *ChemPhysChem* **2003**, *4*, 439–444.
(6) Attfield, J. P. *Solid State Sci.* **2006**, *8*, 861–867.
(7) Zeng, Z.; Greenblatt, M.; Subramanian, M. A.; Croft, M. *Phys. Rev. Lett.* **1999**, *82*, 3164–3167.
(8) Subramanian, M. A.; Li, D.; Duan, N.; Reisner, B. A.; Sleight, A. W. *J. Solid State Chem.* **2000**, *151*, 323–325.
(9) Alonso, J. A.; Sanchez-Benitez, J.; De Andres, A.; Martinez-Lope, M. J.; Casais, M. T.; Martinez, J. L. *Appl. Phys. Lett.* **2003**, *83*, 2623–2625.
(10) Kobayashi, W.; Terasaki, I.; Takeya, J.; Tsukada, I.; Ando, Y. *J. Phys. Soc. Jpn.* **2004**, *73*, 2373–2376.
(11) Prodi, A.; Gilioli, E.; Gauzzi, A.; Licci, F.; Marezio, M.; Bolzoni, F.; Huang, Q.; Santoro, A.; Lynn, J. W. *Nat. Mater.* **2004**, *3*, 48–52.
(12) Bochu, B.; Buevoz, J. L.; Chenavas, J.; Collomb, A.; Joubert, J. C.; Marezio, M. *Solid State Commun.* **1980**, *36*, 133–138.
(13) Prodi, A.; Gilioli, E.; Cabassi, R.; Bolzoni, F.; Licci, F.; Huang, Q. Z.; Lynn, J. W.; Affronte, M.; Gauzzi, A.; Marezio, M. *Phys. Rev. B* **2009**, *79*, 085105.
(14) Bocquet, A. E.; Fujimori, A.; Mizokawa, T.; Saitoh, T.; Namatame, H.; Suga, S.; Kimizuka, N.; Takeda, Y.; Takano, M. *Phys. Rev. B* **1992**, *45*, 1561–1570.
(15) Yamada, I.; Takata, K.; Hayashi, N.; Shinohara, S.; Azuma, M.; Mori, S.; Muranaka, S.; Shimakawa, Y.; Takano, M. *Angew. Chem., Int. Ed.* **2008**, *47*, 7032–7035.
(16) Yamada, I.; Tsuchida, K.; Ohgushi, K.; Hayashi, N.; Kim, J.; Tsuji, N.; Takahashi, R.; Matsushita, M.; Nishiyama, N.; Inoue, T.; Irifune, T.; Kato, K.; Takata, M.; Takano, M. *Angew. Chem., Int. Ed.* **2011**, *50*, 6579–6582.

(17) Yamada, I.; Shiro, K.; Etani, H.; Marukawa, S.; Hayashi, N.; Mizumaki, M.; Kusano, Y.; Ueda, S.; Abe, H.; Irifune, T. *Inorg. Chem.* **2014**, *53*, 10563−10569.
(18) Long, Y. W.; Hayashi, N.; Saito, T.; Azuma, M.; Muranaka, S.; Shimakawa, Y. *Nature* **2009**, *458*, 60−63.
(19) Etani, H.; Yamada, I.; Ohgushi, K.; Hayashi, N.; Kusano, Y.; Mizumaki, M.; Kim, J.; Tsuji, N.; Takahashi, R.; Nishiyama, N.; Inoue, T.; Irifune, T.; Takano, M. *J. Am. Chem. Soc.* **2013**, *135*, 6100−6106.
(20) Yamada, I.; Etani, H.; Tsuchida, K.; Marukawa, S.; Hayashi, N.; Kawakami, T.; Mizumaki, M.; Ohgushi, K.; Kusano, Y.; Kim, J.; Tsuji, N.; Takahashi, R.; Nishiyama, N.; Inoue, T.; Irifune, T.; Takano, M. *Inorg. Chem.* **2013**, *52*, 13751−13761.
(21) Shimakawa, Y.; Takano, M. *Z. Anorg. Allg. Chem.* **2009**, *635*, 1882−1889.
(22) Chen, W.-t.; Long, Y.; Saito, T.; Attfield, J. P.; Shimakawa, Y. *J. Mater. Chem.* **2010**, *20*, 7282−7286.
(23) Sanchez-Benitez, J.; Martinez-Lope, M. J.; Alonso, J. A. *J. Appl. Phys.* **2010**, *107*, 103904.
(24) Kakihana, M. *J. Sol-Gel Sci. Technol.* **1996**, *6*, 7−55.
(25) Izumi, F.; Momma, K. *Solid State Phenom.* **2007**, *130*, 15−20.
(26) Momma, K.; Izumi, F. *J. Appl. Crystallogr.* **2011**, *44*, 1272−1276.
(27) Studer, A. J.; Hagen, M. E.; Noakes, T. J. *Physica B* **2006**, *385*−*86*, 1013−1015.
(28) Ueda, S.; Katsuya, Y.; Tanaka, M.; Yoshikawa, H.; Yamashita, Y.; Ishimaru, S.; Matsushita, Y.; Kobayashi, K. *AIP Conf. Proc.* **2010**, *1234*, 403−406.
(29) Ueda, S. *J. Electron Spectrosc. Relat. Phenom.* **2013**, *190*, 235−241.
(30) Saitoh, Y.; Kimura, H.; Suzuki, Y.; Nakatani, T.; Matsushita, T.; Muro, T.; Miyahara, T.; Fujisawa, M.; Soda, K.; Ueda, S.; Harada, H.; Kotsugi, M.; Sekiyama, A.; Suga, S. *Rev. Sci. Instrum.* **2000**, *71*, 3254−3259.
(31) Brown, I. D.; Altermatt, D. *Acta Crystallogr., Sect. B* **1985**, *41*, 244−247.
(32) Shannon, R. D. *Acta Crystallogr., Sect. A* **1976**, *32*, 751−767.
(33) Shelef, M.; Haack, L. P.; Soltis, R. E.; Devries, J. E.; Logothetis, E. M. *J. Catal.* **1992**, *137*, 114−126.
(34) Steiner, P.; Kinsinger, V.; Sander, I.; Siegwart, B.; Hufner, S.; Politis, C.; Hoppe, R.; Muller, H. P. *Z. Phys. B* **1987**, *67*, 497−502.
(35) Goodenough, J. B. *Magnetism and Chemical Bond*; Wiley: New York, 1963.
(36) Long, Y.; Saito, T.; Mizumaki, M.; Agui, A.; Shimakawa, Y. *J. Am. Chem. Soc.* **2009**, *131*, 16244−16247.
(37) Li, J. Q.; Matsui, Y.; Park, S. K.; Tokura, Y. *Phys. Rev. Lett.* **1997**, *79*, 297−300.